

Roles of Nanoscale Defects of Graphene in Remote Epitaxy of GaN

Jeongwoon Kim, Hyeon Woo Kim, Jongil Kim, Je-Sung Lee, Hoe-Min Kwak, Jaeyoung Baik, Soo-Young Choi, Jinsoo Kim, Si-Young Bae, Sang-Jo Kim, Jun-Youn Kim, Il Jeon, Sung Beom Cho, Sang Ho Oh, Young Joon Hong,* and Dong-Seon Lee*

Remote epitaxy through graphene enables the fabrication of freestanding membranes, facilitating the “peel-and-stack” process for semiconductor hetero-integration. While previous studies have emphasized graphene thickness, substrate bonding ionicity, and damage-free transfer of graphene for implementing remote epitaxy, the impact of nanoscale microscopic defects in graphene remains unexplored. Metal–organic chemical vapor deposition (MOCVD) of GaN requires high temperatures and a radical reaction environment, which can damage graphene. This study investigates the effects of chemical doping and nanoscale defects in graphene on remote epitaxy during MOCVD growth of GaN crystallites on graphene-coated Al₂O₃ for understanding the early growth stage and the resulting crystal quality. Three distinct modes are identified: remote epitaxy, anchored remote epitaxy, and epitaxial lateral overgrowth (ELOG). Pristine graphene enables pure remote epitaxy of well-aligned, strain-relaxed GaN crystallites. N-doped graphene promotes chemically anchored nucleation, causing slightly misaligned crystallites due to altered remote atomic interaction, newly termed “anchored remote epitaxy”. Graphene pinholes induce direct GaN–Al₂O₃ covalent bonding for ELOG, resulting in significant compressive strain in GaN. How graphene’s chemical and physical defects affect epitaxial crystallite quality (i.e., alignment, strain relaxation, density) is further explored based on bonding mechanisms, providing insights into remote epitaxy for next-generation semiconductor fabrication.

1. Introduction

Epitaxy is the process of forming an atomically ordered overlayer on a substrate, driven by forming covalent bonding with unsaturated surface atoms.^[1] The atomic ordering is governed by microscopic parameters of bond length, angle, and strength, as well as physical parameters of crystal symmetry and lattice mismatch. Achieving a high-quality epilayer requires selecting materials that align with these optimal parameters. Recently, remote epitaxy has emerged with a breakthrough in semiconductor thin-film growth^[2–5]: unlike conventional epitaxy, this approach enables the growth of high-quality epilayers, as the noncovalent interface at the epilayer/substrate offers a greater degree of freedom from the aforementioned deterministic parameters. The absence of covalent bonding also allows easy mechanical delamination of epilayers.^[6–11] In particular, weak interfacial bonding facilitates the spontaneous relaxation of strain induced by lattice mismatch in the epitaxial layer.

J. Kim, J.-S. Lee, J. Baik, S.-Y. Choi, J. Kim, D.-S. Lee
 School of Electrical Engineering and Computer Science
 Department of Semiconductor Engineering
 Gwangju Institute of Science and Technology (GIST)
 Gwangju 61005, Republic of Korea
 E-mail: dslee66@gist.ac.kr

H. W. Kim, S. B. Cho
 Department of Materials Science and Engineering
 Department of Energy Systems Research
 Ajou University
 Suwon 16499, Republic of Korea

 The ORCID identification number(s) for the author(s) of this article can be found under <https://doi.org/10.1002/smll.202503428>
 © 2025 The Author(s). Small published by Wiley-VCH GmbH. This is an open access article under the terms of the [Creative Commons Attribution-NonCommercial License](#), which permits use, distribution and reproduction in any medium, provided the original work is properly cited and is not used for commercial purposes.

DOI: [10.1002/smll.202503428](https://doi.org/10.1002/smll.202503428)

J. Kim, S. H. Oh
 Department of Energy Engineering
 Institute for Energy Materials and Devices
 Korea Institute of Energy Technology (KENTECH)
 Naju 58330, Republic of Korea
 H.-M. Kwak
 Thin GaN Material & Device Creative Research Section
 Electronics and Telecommunications Research Institute (ETRI)
 Daejeon 34129, Republic of Korea
 S.-Y. Bae
 Major of Semiconductor Engineering
 Division of Nanotechnology and Semiconductor Engineering
 Pukyong National University
 Busan 49315, Republic of Korea
 S.-J. Kim, J.-Y. Kim
 Samsung Display Co.
 Yongin 17113, Republic of Korea

In conventional covalent-based heteroepitaxy, strain is typically relaxed through the formation of misfit dislocations.^[12] In contrast, in remote epitaxy, the energy required to form dislocations at the epilayer/two-dimensional material (2dM) interface is significantly higher than the energy required for lattice displacement at the interface.^[13–15] As a result, dislocation formation is suppressed. This characteristic enables the growth of nearly dislocation-free epitaxial layers even under heteroepitaxial systems, such as GaP on GaAs ($\approx 3.7\%$) and GaN on Al_2O_3 (-16.1%).^[13–17]

The driving forces behind 2dM-assisted epitaxy (i.e., remote epitaxy and van der Waals (vdW) epitaxy) include remote interactions induced by the substrate and vdW attraction from the 2dM.^[18–21] For remote epitaxy, the substrate's remote interaction dominates, dictating the epitaxial relationship.^[18,22] This remote epitaxial interaction, arising from the bonding ionicity, generates surface-localized charge, attracting adatoms through the 2dM to form the epilayer.^[19,23–25] However, this attraction is significantly weaker than covalent bonding, imposing other stringent requirements for successful remote epitaxy. These include precise 2dM thickness (e.g., maximum 1 monolayer (ML) graphene for GaAs, 2 MLs for GaN, 3 MLs for ZnO),^[18,26] sufficient bonding ionicity or polarity of the substrate, and a damage-free 2dM transfer.^[27,28] Particularly, a pristine 2dM layer with a clean and abrupt 2dM/substrate interface is essential to ensure the undisturbed remote epitaxial interaction.^[28,29] Despite advances in understanding these mechanisms, the effects of chemical doping and nanoscale defects in 2dMs on remote epitaxy mechanisms and the epilayer quality remain insufficiently explored. In vdW epitaxy, defects in graphene can introduce dangling bonds that promote the nucleation of GaN or provide stable nucleation sites, thereby improving the crystalline quality of the epilayer.^[20,30] Additionally, chemical bonding at the interface can influence the polarity of the GaN film.^[31] However, these findings have primarily focused on the direct interaction between the epilayer and the 2dM, while the role of remote interaction has not been adequately considered. To achieve high-quality epitaxial films via remote epitaxy, it is essential to examine the combined effects of remote interaction and graphene defects, particularly regarding their influence on initial growth behavior and defect formation processes.

GaN, a wide-bandgap semiconductor with a direct gap of 3.4 eV, offers complete compositional tunability with InN and AlN, spanning bandgap from 0.7 to 6.2 eV, which includes wide range light spectra from far infrared to ultraviolet-C.^[32] In addition, its superior electrical properties, including a high breakdown field ($3.3 \times 10^6 \text{ V cm}^{-1}$) and high saturated electron velocity ($> 10^7 \text{ cm s}^{-1}$), make it indispensable for applications in full-color light-emitting diode displays, laser

diodes, radio-frequency amplifiers, high-electron-mobility transistors (HEMTs), and high-power transistors.^[33,34] These attributes have positioned GaN as one of the important materials for multi-functional heterogeneous integration.^[35,36] To this end, the preparation of freestanding, stackable GaN membranes is essential, since the high temperatures required for GaN growth exceed the thermal stability limits of silicon-based electronics.^[37] Moreover, conventional lift-off techniques, such as laser lift-off and chemical etching, for the release of GaN epilayer encounter formidable obstacles in achieving damage-free, high-yield, and rapid lift-off processes for membrane production.^[38–41] Remote epitaxy through graphene presents a promising technique for damage-free, high-quality free-standing membrane preparation.^[5–7,42]

Graphene, an sp^2 -bonded elemental material layer without a permanent dipole, is an ideal 2dM layer for remote epitaxy. Furthermore, well-established, large-area graphene growth techniques allow precise thickness control in mass production.^[43] Despite its advantages, graphene's volatility and instability, especially on GaN and AlN substrates due to thermochemical decomposition under metal-organic chemical vapor deposition (MOCVD) conditions of high temperatures ($> 1000^\circ\text{C}$) and reactive gases (e.g., NH_3 , H_2) for GaN growth, pose critical challenges:^[44–49] graphene on III-nitride substrates forms graphitic and pyridinic nitrogen defects in graphene because outgassed nitrogen from substrate easily reacts with graphene.^[40,46] Graphene on Al_2O_3 is more thermally stable, but it still suffers damage under the NH_3 - and H_2 -rich conditions at high temperature.^[50] Hence, this thermochemical instability motivates efforts to control defect formation in graphene, not only to ensure the integrity of remote epitaxy but also to unlock its potential for developing new graphene-assisted epitaxy modes for broader applications.

Herein, we report the influence of nanoscale physical and chemical defects in graphene on remote epitaxy of GaN on Al_2O_3 . This study primarily focuses on the initial growth stage, prior to the formation of a continuous thin film, as the isolated island structures observed at this stage provide critical and direct evidence for understanding the origin of crystal orientation distribution and strain evolution. By adjusting MOCVD thermal pretreatment and growth conditions, we induced nitrogen doping and pinhole openings in graphene. Depending on graphene's defect state, epitaxy was classified into three regimes: remote epitaxy, anchored remote epitaxy, and epitaxial lateral overgrowth (ELOG). We examined the key characteristics of epitaxy (i.e., nucleation, crystallographic alignment, and strain relaxation) in relation to graphene defects for the three epitaxy regimes. Scanning and transmission electron microscopies (SEM and TEM), x-ray diffraction (XRD), and electron energy loss spectroscopy (EELS) were used to analyze GaN and interfacial microstructures, while atomic force microscopy (AFM) and Raman spectroscopy characterized the graphene quality and surface properties. To elucidate the mechanisms of remote and anchored remote epitaxy, density-functional theory (DFT) computational simulations of charge density re-distribution on graphene were performed for graphene-coated Al_2O_3 substrates with vacancy and various types of nitrogen doping in graphene.

I. Jeon, Y. J. Hong
Department of Nano Engineering
Department of Nano Science and Technology
SKKU Advanced Institute of Nanotechnology (SAINT)
Sungkyunkwan University
Suwon 16419, Republic of Korea
E-mail: yjhong78@skku.edu

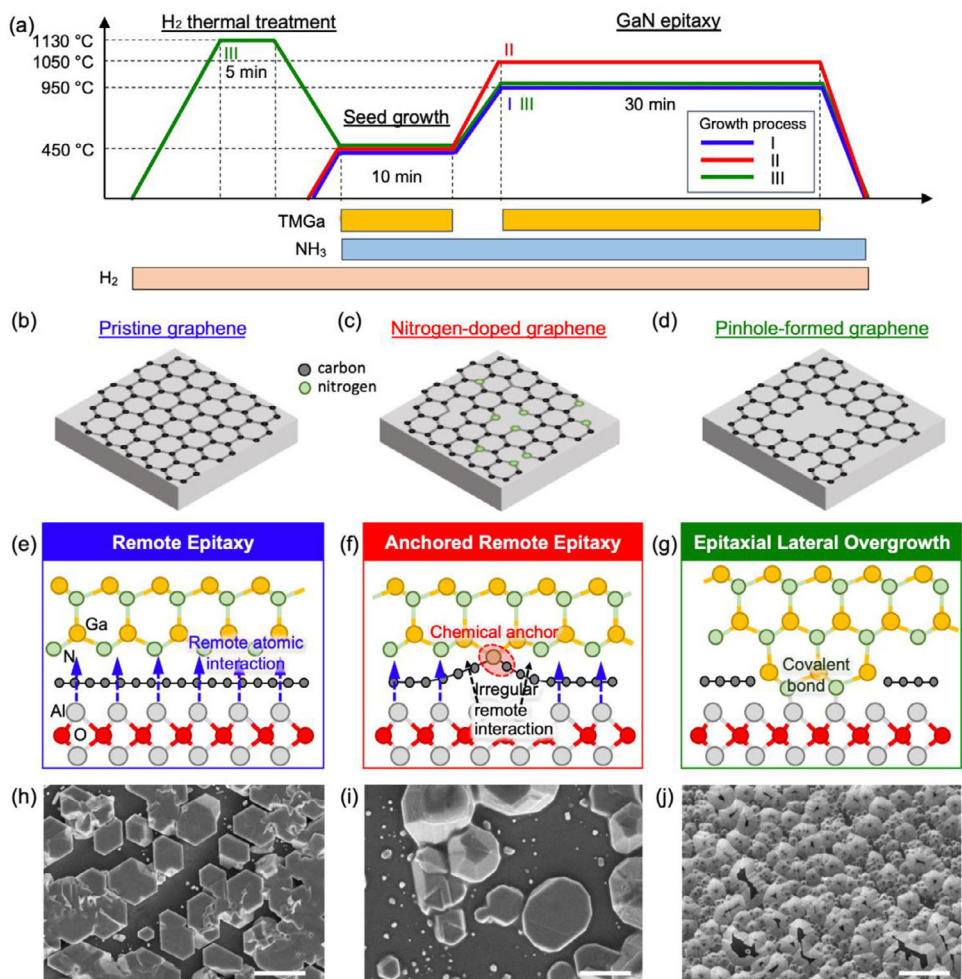


Figure 1. Graphene-assisted epitaxy of GaN on graphene-coated Al_2O_3 . a) Temperature and gas injection profiles of MOCVD for remote epitaxy (blue line, growth process I), anchored remote epitaxy (red line, growth process II), and epitaxial lateral overgrowth (ELOG, green line, growth process III). b–d) Schematic illustrations of Al_2O_3 substrates coated with pristine graphene (b), nitrogen-doped graphene (c), and pinhole-formed graphene (d). e–g) Cross-sectional illustrations representing the interface structure and bonding types. h–j) Plan-view SEM images of GaN crystallites formed on graphene-coated Al_2O_3 substrate by remote epitaxy, anchored remote epitaxy, and ELOG (from left to right). Scale bars of the SEM images correspond to 5 μm .

2. Results and Discussion

2.1. Three Epitaxy Modes Dependent on Defects in Graphene

The epitaxy modes were investigated by growing micron-sized GaN crystallites on graphene-coated $\alpha\text{-Al}_2\text{O}_3(0001)$ substrate via MOCVD. Spatially isolated GaN crystallites, instead of forming continuous thin films, were grown for an intuitive evaluation of their crystallographic orientation after an initial growth stage and overall epitaxial relationship. Various ambient gases and annealing temperatures were employed to modify the graphene surface in different ways and distinguish between epitaxy modes (Figure 1a,b). For substrate preparation, single-layer graphene with a typical domain size of 5–20 μm was synthesized via chemical vapor deposition (CVD) on Cu foil and transferred onto Al_2O_3 substrate using the poly(methyl methacrylate)-supported wet-transfer technique.^[51] Detailed procedures are provided in the Experimental section.

Figure 1a outlines the temperature profiles and injection procedures of gases and precursors used for graphene treatment and epitaxial GaN growth. Three distinct epitaxy modes of GaN–remote, anchored, and lateral overgrowth epitaxy—were identified, each determined by the type of graphene defects induced by thermal treatment (Figure S1 and Note S1, Supporting Information). Depending on the treatment, we obtained three representative graphene types: pristine, nitrogen-doped, and pinhole-formed, as schematically depicted in Figure 1b–d. The epitaxy of GaN was performed at temperatures above 950 °C for 30 min, following a seed growth step at 450 °C for 10 min.

2.1.1. Remote Epitaxy (Growth Process I)

Without thermal pretreatment, graphene remained pristine at a growth temperature of 950 °C, enabling the formation of

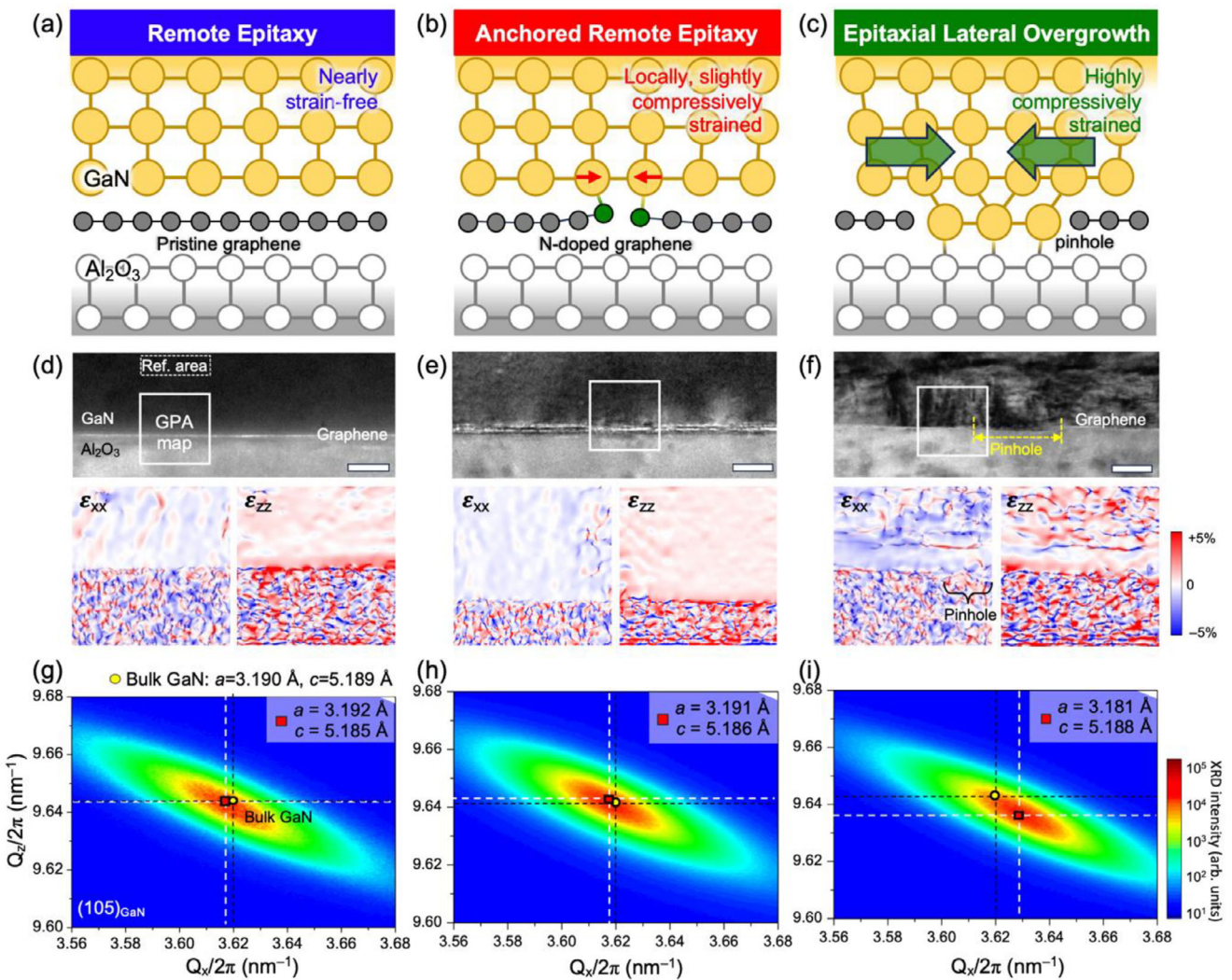


Figure 2. Strain in GaN. a–c) Cross-sectional schematics illustrating strain induced by different bonding types in GaN epi-layer for remote epitaxy (a), anchored remote epitaxy (b), and ELOG (c). d–f) Cross-sectional HR-TEM images (top, scale bars: 20 nm) and geometric phase analysis (GPA) strain maps along in-plane and out-of-plane directions (bottom) for remote epitaxy, anchored remote epitaxy, and ELOG (from left to right). The GPA maps correspond to the boxed regions marked in the TEM images. g–i) The corresponding XRD HL-mesh contour reciprocal space maps (RSMs) of (105)_{GaN} (right) for GaN grown by remote epitaxy, anchored remote epitaxy, and ELOG (from left to right). Measured peak positions are marked with red squares, along with the calculated lattice constant values, while the strain-free bulk GaN value is marked with yellow circles for comparison.

well-aligned hexagonal prismatic GaN crystallites on graphene/Al₂O₃ substrate (Figure 1h). The nucleation density was $\approx 1.7 \times 10^7 \text{ cm}^{-2}$, assuming each nucleus developed into visible crystallites in SEM images (Figure S2 and Notes S1, Supporting Information). Complementary TEM, AFM, and Raman spectroscopy measurements confirmed that the single-layer graphene remained undamaged without significant nanoscale physical defects before and after GaN growth (Figure 2d; Figure S3, Supporting Information), signifying “remote epitaxy” through pristine graphene. As schematically depicted in Figure 1e, no covalent bonds were mediated at the GaN/graphene/Al₂O₃ interface during this growth. Remote epitaxy is driven by atomic interaction remotely transmitted through graphene, where the diametrically aligned p_z orbitals of pristine graphene mediate charge transfer from Al₂O₃ to the surface along the z-direction. This remote epitaxial interaction,

exhibiting periodic cationic and anionic characteristics, appears undisturbed on graphene (Figure 5b). Thus, maintaining the integrity of graphene is essential for achieving remote epitaxy.

2.1.2. Anchored Remote Epitaxy (Growth Process II)

Increasing the growth temperature to 1050 °C resulted in a mixture of well-aligned and less-aligned GaN crystallites on nitrogen-doped graphene (Figure 1i). TEM, AFM, and Raman spectroscopy confirmed that the graphene remained physically undamaged but became doped with nitrogen (Figure 1c, Figure 2e; Figure S3 and Note S2, Supporting Information), likely due to NH₃ cracking at elevated growth temperature, which provided sufficient activation energy for nitrogen incorporation.^[52] We propose that N-doped graphene led to localized chemical

Table 1. Three representative graphene-assisted GaN epitaxy modes on c-Al₂O₃ substrate.

Epitaxy Mode	Remote Epitaxy	Anchored Remote Epitaxy	ELOG
Graphene defect	Nearly pristine	Nitrogen doping (<1 at.%)	Pinhole (several tens nm)
Interface bonding	Remote epitaxial interaction	Chemical anchoring (or bonding) between GaN and N-doped graphene, ^{a)} pure and disturbed remote interaction	Covalent bond with substrate
In-plane orientation	Aligned	Aligned (~74%) <5°-rotated (~26%) ^{a)}	Aligned
Out-of-plane orientation	Aligned	Aligned	Slightly tilted (around the pinhole)
Strain relaxation (measured by GPA)	-0.18%	-0.32%	-0.63%

^{a)} Small-angle-misaligned crystallites are grown from N-doped graphene.

anchoring of adatoms, initiating the nucleation of slightly misaligned GaN, followed by subsequent growth (Figure 1f). This suggests that chemical anchoring between GaN and N-doped graphene disrupts the ideal remote epitaxy mechanism with irregular remote interaction (Figure 1f), introducing a secondary remote epitaxy pathway. To describe this phenomenon, we introduce the term “anchored remote epitaxy.” Partially N-doped graphene (ca. <1%, Figure S3 and Note S2, Supporting Information) thus induces a mixed growth regime, incorporating elements of both pure remote and anchored remote epitaxy. For convenience, we refer to this regime simply as anchored remote epitaxy throughout this article. The nucleation density was measured at $\approx 2.8 \times 10^7 \text{ cm}^{-2}$, which is higher than that observed in remote epitaxy, due to the higher sticking probability of adatoms on N-doped sites.

2.1.3. Epitaxial Lateral Overgrowth (Growth Process III)

This epitaxy mode was achieved by introducing a thermal pre-treatment step to Growth Process I (Figure 1a). Growth Process III resulted in well-aligned, high-density hexagonal pyramids (Figure 1j), distinct from those of remote epitaxy by Growth Process I, despite identical seed and epitaxial growth conditions. A hydrogen-rich thermal treatment at 1130 °C created numerous pinhole openings in the graphene (Figure 1d), several tens of nanometers in size, as confirmed by AFM (Figure S3, Supporting Information). Additionally, Raman spectroscopy and TEM measurements further supported this observation (Figure S3 and Note S2, Supporting Information). The number density of pinholes ($3.4 \times 10^7 \text{ cm}^{-2}$, Note S1, Supporting Information) matched the pyramid density ($3.7 \times 10^7 \text{ cm}^{-2}$) in nearly one-to-one correspondence. Thus, GaN pyramids nucleated via direct epitaxy through nanoscale pinholes in graphene, followed by epitaxial lateral overgrowth (ELOG), as illustrated in Figure 1g.

The above three distinct graphene-assisted GaN epitaxy modes on c-Al₂O₃ exhibit clear differences in graphene defect types, interfacial bonding, crystallographic orientation, and strain relaxation, highlighting the critical role of graphene’s interfacial state in determining epitaxial behavior (Table 1).

2.2. Strain Relaxation Through Graphene

Three epitaxy modes exhibited different strain relaxation characteristics, determined by their epitaxial bonding types

(Figure 2a–c). Cross-sectional HR-TEM confirmed the presence of single-layer graphene between GaN and Al₂O₃ across all growth processes (Figure 2d–f). In remote epitaxy, the GaN/graphene interface appeared abrupt and clean (Figure 2d). In contrast, anchored remote epitaxy exhibited non-uniform contrast, particularly at the bottom of GaN, likely due to localized interface defects or strain (Figure 2e). In ELOG, pronounced partial contrast variations were observed, attributed to highly strained internal lattices within the GaN crystallites (Figure 2f).

Strain in GaN was quantitatively characterized by mapping ϵ_{xx} (in-plane strain) and ϵ_{zz} (out-of-plane strain) using geometrical phase analysis (GPA) from high-resolution STEM images (lower panels in Figure 2d–f). It should be noted that the GPA analysis was performed on the bottom 20–30 nm of GaN, where strain is highly sensitive to bonding and interactions with the substrate. For relative comparison, the reference region was selected from the remote epitaxial layer away from the interface, as marked in Figure 2d. Then, mapping analyses of ϵ_{xx} and ϵ_{zz} were performed to calculate the average lattice constant differences $\Delta a/a_{\text{reference}}$ (for in-plane) and $\Delta c/c_{\text{reference}}$ (for out-of-plane). Both remote and anchored remote epitaxial GaN crystallites exhibited slightly in-plane compressive strain and out-of-plane tensile strain. The average ϵ_{xx} values for remote and anchored remote epitaxy were -0.18% and -0.32%, respectively (Figure 2d,f). The minor compressive strain in remote epitaxy is attributed to weak remote epitaxial interaction across the non-covalent interface. The slightly greater compressive strain in anchored remote epitaxial GaN results from chemical anchoring, which strengthens interfacial binding at the GaN/graphene interface. However, the strain remained relatively low, presumably due to the absence of direct bonds with Al₂O₃. For ELOG GaN, a more substantial compressive strain was observed, with a mean ϵ_{xx} value of -0.63%. This strain was particularly pronounced specifically near pinhole regions (-0.93%, Figure S5, Supporting Information), a consequence of the large lattice mismatch between GaN and Al₂O₃.

The lattice constants a and c of the GaN crystallites were determined by measuring the XRD reciprocal space map (RSM) peak of the (105)_{GaN} diffraction. Unlike TEM, XRD provides statistically significant data by capturing lattice information across the entire measured volume. For remote epitaxy, the lattice constants were $a = 3.192 \text{ \AA}$ and $c = 5.185 \text{ \AA}$, with the a value being 0.06% larger and the c value 0.07% smaller than those of single-crystal bulk GaN ($a = 3.190 \text{ \AA}$, $c = 5.18 \text{ \AA}$).^[53] Similarly, anchored remote epitaxy showed almost similar lattice constants,

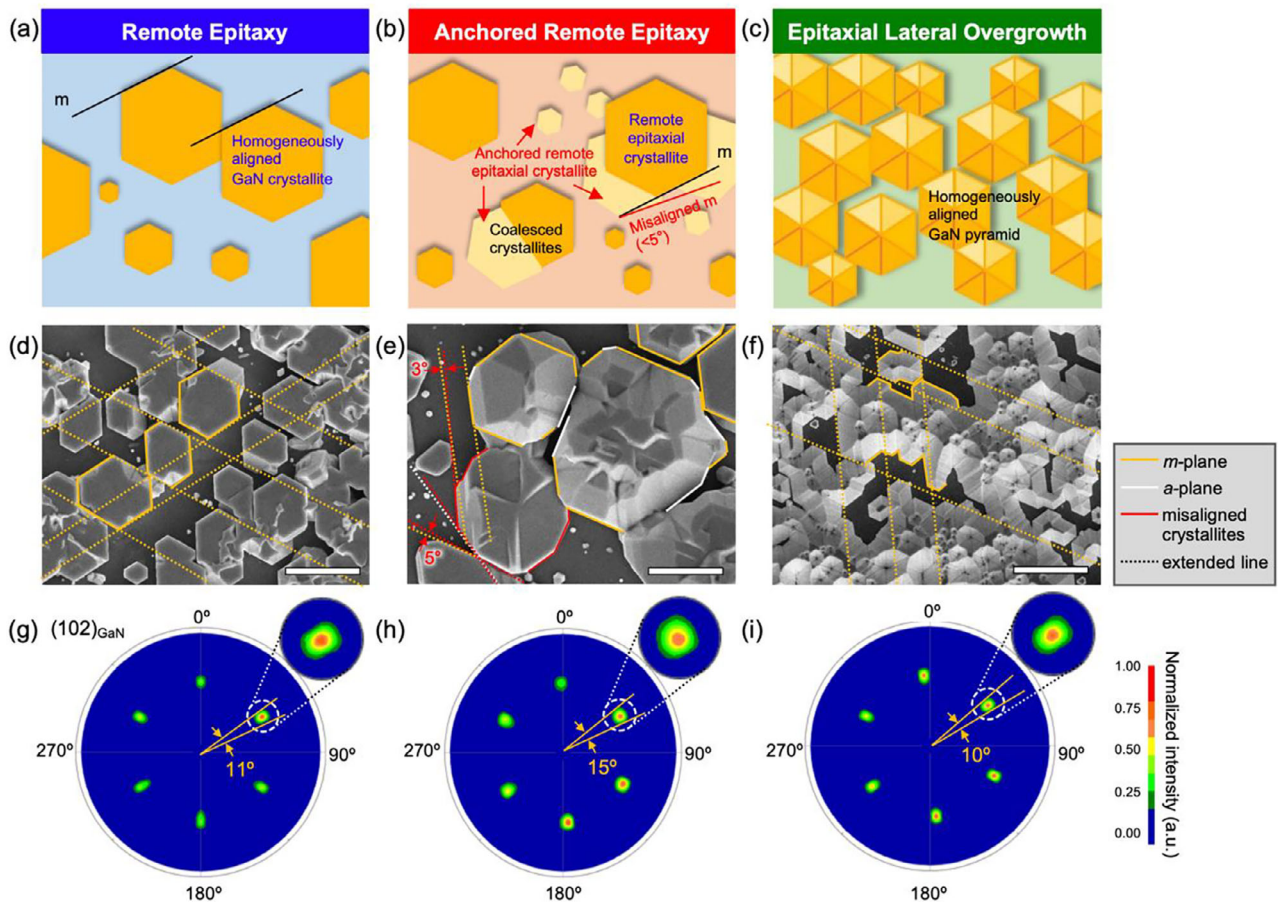


Figure 3. In-plane epitaxial alignment. a–c) Top-view schematics, d–f) corresponding plan-view SEM images, and g–i) XRD pole figure scan maps measured from GaN crystallites grown by remote epitaxy (a,d,g), anchored remote epitaxy (b,e,h), and ELOG (c,f,i). The pole figure was measured for (102)_{GaN}, showing six-fold rotational symmetry. Insets in (g–i) show enlarged peaks from the pole figure maps. Scale bars in SEM images correspond to 5 μm. Peak widths in (g–i) were measured using the null-to-null width method.

with $a = 3.191 \text{ \AA}$ and $c = 5.186 \text{ \AA}$. In contrast, ELOG exhibited lattice constants of $a = 3.181 \text{ \AA}$ and $c = 5.188 \text{ \AA}$, with the in-plane a value 0.28% smaller than that of bulk GaN, indicating highly compressive in-plane strain, even though our ELOG was performed on nanoscale pinhole openings. Nevertheless, it is noteworthy that the strain in graphene-assisted ELOG GaN (-0.28%) was more relaxed than that of conventional epitaxial GaN on Al_2O_3 (-0.37%).^[54,55] Both TEM-GPA and XRD measurements confirmed that remote and anchored remote epitaxy facilitated efficient strain relaxation, whereas ELOG exhibited strained epitaxial crystallites due to direct GaN– Al_2O_3 covalent bonding through graphene pinholes. Among the three epitaxy modes, remote epitaxy exhibited the most effective strain relaxation, implying the critical role of weak interfacial bonding between the GaN epilayer and graphene. The reduced internal strain within the membrane, attributed to the weak remote interaction, could facilitate the fabrication of high-quality, freestanding GaN membranes. In conventional heteroepitaxy of GaN, thick strain-relief layers are typically required to substantially accommodate a large lattice mismatch between the epilayer and the substrate. In contrast, remote epitaxy utilizes the non-covalent interaction with

graphene to decouple strain transfer from the substrate, which effectively replaces the need for additional strain-relief layers. This approach holds great promise for producing thinner, more flexible, and high-quality GaN membranes, compared to traditional epitaxial membrane fabrication techniques.

2.3. In-Plane Epitaxial Alignment

Since the epitaxial alignment of the crystallites is determined during nucleation and the early growth stage, observing the in-plane alignment distribution of crystallites provides a basic insight into the initial epitaxial relation. As shown in the schematics and SEM images, remote epitaxy produced several-micron-sized, well-aligned hexagonal prismatic GaN crystallites with vertical sidewalls, despite the use of polycrystalline graphene (Figure 3a,d). Anchored remote epitaxy resulted in a mixture of well-aligned (74%) and less-aligned (26%) GaN crystallites, with the misaligned crystallites rotated by less than $\pm 5^\circ$ relative to the well-aligned majority (Figure 3b,e). Some crystallites were observed to coalesce. Although nitrogen doping in graphene was estimated to be just less than one atomic % of graphene (Figure S3

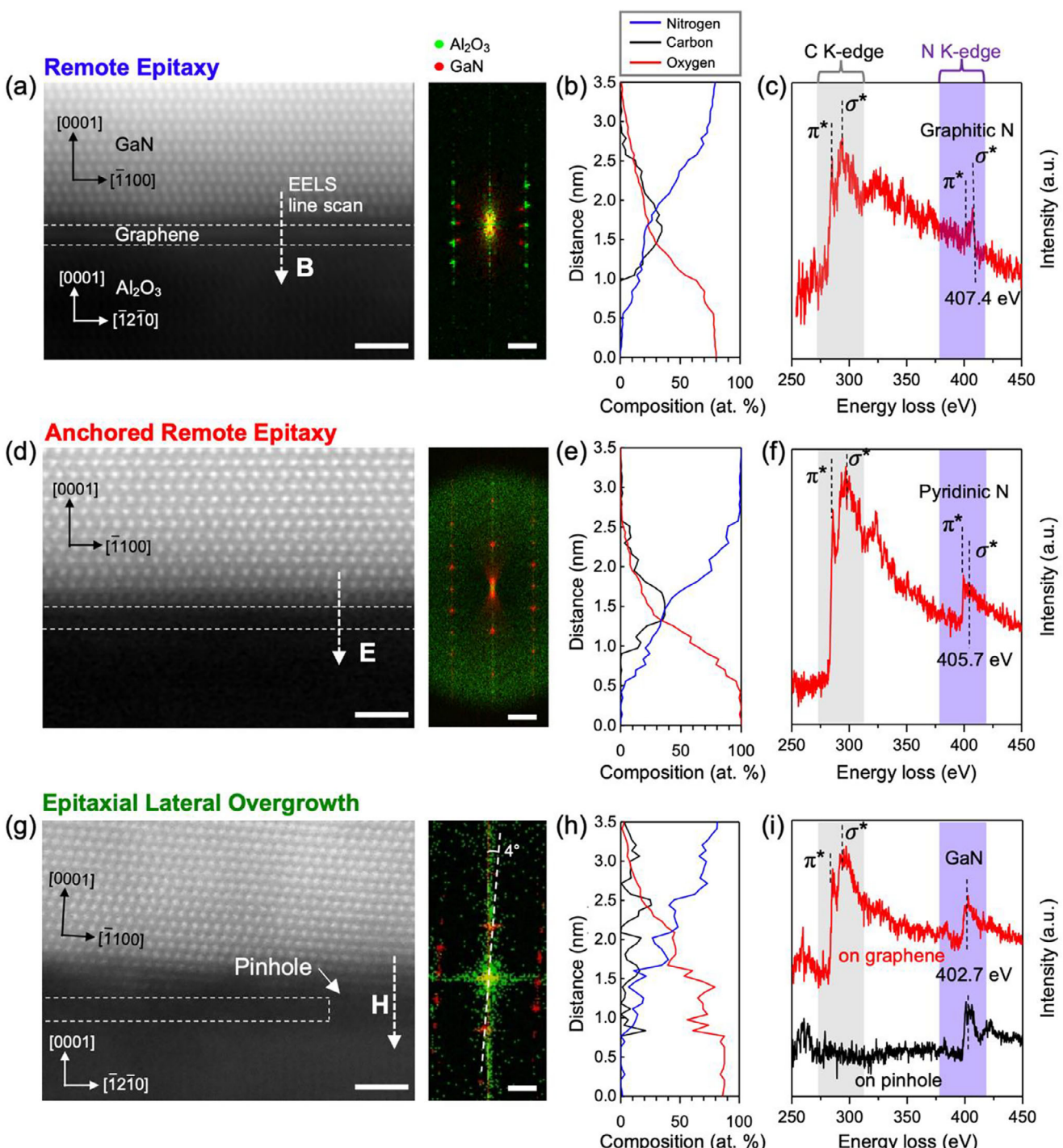


Figure 4. Out-of-plane epitaxial relation and chemical states of graphene. a,d,g) High-resolution cross-sectional STEM images (left) and corresponding fast-Fourier transform (FFT) diffraction patterns (right) of GaN grown on graphene-coated Al_2O_3 by remote epitaxy (a), anchored remote epitaxy (d), and ELOG (g). b,e,h) EELS line profiles scanned along the dotted-line arrows marked in the STEM images. c,f,i) EELS spectra locally recorded from the graphene (or pinhole) region at C K- and N K-edges. Scale bars for STEM and FFT images are 2 nm and 2 nm⁻¹, respectively.

and Note S2, Supporting Information), less-aligned crystallites in anchored remote epitaxy accounted for 26% of the total. This suggests that N-doped graphene sites with unsaturated electron pairs drove high-density nucleation and growth of misaligned crystallites. Furthermore, this misalignment is attributed to the

disruption of remote atomic interactions. Meanwhile, ELOG produced well-aligned hexagonal pyramids with no significant misalignment.

The epitaxial relationship was evaluated using XRD pole figure measurements of the $(102)_{\text{GaN}}$ Bragg reflection. All

epitaxy modes exhibited six-fold rotational symmetry (Figure 3g–i; Figure S6, Supporting Information), with no additional peaks or ring-shaped tails, indicating a robust epitaxial relationship between GaN and Al₂O₃. However, anchored remote epitaxy exhibited the broadest pole figure peaks with a width of 15°, measured by the null-to-null width method, along the circumferential direction compared to remote epitaxy (11°) and ELOG (10°) (inset of Figure 3g–i), due to the slight in-plane misalignment distributions. This observation is consistent with the plan-view SEM analysis.

2.4. Interface Structure and Chemical Analysis of GaN/Graphene/Al₂O₃

The interface structures and chemical states of graphene were investigated using STEM and EELS. Cross-sectional STEM images (Figure 4a,d,g) and EELS line profiles (Figure 4b,e,h) also confirmed the presence of the graphene layer at the GaN/graphene/Al₂O₃ interface across all samples. However, significant structural and chemical differences were observed.

For both remote and anchored remote epitaxy, the single-layer graphene was observed intact without direct structural linkage between GaN and Al₂O₃ (Figure 4a,d). In contrast, in the ELOG sample, the graphene layer was locally discontinuous due to pinhole openings (Figure 4g). Interestingly, the bottom lattice planes of GaN crystallites grown by remote and anchored remote epitaxy were atomically flat, whereas those in the ELOG sample exhibited a tilted basal plane, with a *c*-axis tilt of ≈4°. This crystallographic tilt is known to alleviate lattice mismatch strain through edge dislocation bending or plastic deformation, as influenced by a mask layer in the conventional ELOG.^[56–58]

Fast Fourier transform (FFT) analysis for the electron diffraction pattern revealed that, in remote epitaxy, GaN and Al₂O₃ were crystallographically well-aligned in both in-plane and out-of-plane directions, following the relationship (0001)[−1100]_{GaN} || graphene || (0001)[−12−10]_{sapphire} (Figure 4a). However, in anchored remote epitaxy, slight in-plane misalignment was observed (Figure 4d), as the zone axes of GaN and Al₂O₃ did not align due to in-plane orientational incongruities between the two materials. Aligning the GaN zone axis required rotating the sample to bring the Al₂O₃ zone axis into view (Figure S4, Supporting Information), a phenomenon observed only in anchored remote epitaxial GaN. This in-plane epitaxial misalignment likely resulted from chemical anchoring between GaN and N-doped graphene. This observation is consistent with the plan-view SEM analysis in Figure 3e.

Chemical states of graphene were investigated by focusing the electron beam on the graphene regions during the EELS measurements. In remote epitaxy, the π* and σ* bonds were observed at 284.9 and 293.1 eV, respectively, at the C K-edge (Figure 4c), showing no significant deviation from those of pristine graphene reported elsewhere (Table 2).^[59,60] At the N K-edge, π* and σ* bonds appeared as extremely weak peaks at 403.1 and 407.4 eV, barely detectable, indicating a trace amount of nitrogen in the form of graphitic N. Considering the Raman analyses (Figure S3, Supporting Information), the graphitic N doping level in Growth Process I was insignificant. In anchored remote epitaxy, the π* bond at the C K-edge exhibited a blue shift of ≈2 eV, closely

matching the value of stand-alone pyridinic N-doped graphene (Figure 4f). Additionally, the π* and σ* bonds at the N K-edge shifted to lower energies, appearing at 400.1 and 405.7 eV, respectively (Table 2; Figure S7, Supporting Information), strongly suggesting substantial nitrogen doping in the form of pyridinic N.^[59] The σ* bond of pyridinic N graphene after anchored remote epitaxy showed a red shift compared to pristine graphene shown in Figure 4c, attributable to chemical anchoring with GaN, as EELS red shift indicates increased electron density through chemical bonds (Figure S6, Supporting Information).^[61] For ELOG, the EELS analyses were conducted on both graphene-covered and pinhole regions. In the pinhole region, no C K-edge peaks were detected, while the N K-edge peak at 402.7 eV matched the EELS signature of GaN (Figure 4i).^[62] This confirms the direct formation of GaN on Al₂O₃ through the pinhole openings. Meanwhile, the graphene-covered regions exhibited clear C K-edge peaks (Figure 4i).

2.5. Impact of Nanoscale Defects in Graphene on Remote Epitaxial Interactions

So far, we have examined the practical effects of graphene doping and opening on GaN epitaxy. However, to better understand how remote epitaxial interactions are established and how they are altered by defects and doping, we conducted density functional theory (DFT) simulations. These calculations were used to model the charge density (ρ) distributions in the substrate of single-layer graphene on Al₂O₃, providing fundamental understanding into charge transfer mechanisms at the interface for remote epitaxy and anchored remote epitaxy.

Figure 5a presents the DFT-simulated atomic configuration along with 3-D isosurface plots of ρ difference ($\Delta\rho$, also referred to as CDD). The average graphene-Al₂O₃ distance was calculated to be 3.0 Å (Figure 5c). The surface ρ distributions were visualized through contour plotting of the CDD on the graphene surface at a height of 0.9 Å (Figure 5b and mid panels of Figure 5d–i). The plan-view CDD contour map on pristine graphene/Al₂O₃ reveals a periodic charge transfer pattern, forming alternating triangular regions of localized positive (blue) and negative (red) charge (Figure 5b). The cross-sectional CDD contour map shows that positive (cationic) charge is localized on C atoms directly above Al cations in Al₂O₃, while negative (anionic) charge appears on C atoms positioned over O anions (see white and black dotted lines in Figure 5c). These periodically alternating patterns indicate that the localized charge distribution of the Al₂O₃ surface is transmitted to the pristine graphene surface, mediated by the diametrically aligned p_z orbitals of graphene due to their close proximity. This ability of pristine graphene to replicate the underlying substrate's ρ distribution along the z -direction facilitates the periodicity of remote atomic interactions, enabling remote epitaxy with uniformly well-aligned crystallites.^[25]

When a single vacancy was introduced into the graphene, the surface ρ distribution deviated from the periodic pattern, as shown in the plan-view CDD contour map of Figure 5d. The cross-sectional CDD contour map revealed that while the cationic ρ features were well preserved on C-on-Al, the anionic ρ associated with C-on-O sites was significantly disrupted, shifting

Table 2. Summary of EELS peak positions shown in Figure 4c,f,i and comparison with values reported in refs. [60] and [62].

Edges	Bonds	This Work			Other Works			
		Mode I (remote epitaxy)	Mode II (anchored remote epitaxy)	Mode III (ELOG) ^{a)}	Pristine graphene ^[60]	N-doped graphene ^[60]	GaN ^[62]	
C K-edge	π^* bond	284.9	286.8	285.6	285.0	285.5	286.5	—
	σ^* bond	293.1	293.0	292.6	292.7	—	292.7	—
N K-edge	π^* bond	403.1	400.1	402.7	—	401.4	398.0	402.5
	σ^* bond	407.4	405.7	—	407.6	406.6	—	—

^{a)} Data were recorded from the graphene layer region, not from the pinhole region.

to exhibit positive charge instead. N-doping in graphene was further modeled as pyridine or pyrrole structures (Figure 5e–i). The N-doped sites severely broke the periodicity of ρ patterns (see black boxes in plan-view CDD maps of Figure 5e–i). Notably, pyridinic N-doped sites showed anionic characteristics, which could attract Ga cations during the initial nucleation stage, leading to chemical bonding (or anchoring) between Ga atoms and doped nitrogen atoms. It is surmised that this chemical anchoring determines the bonding angle, length, and strength of Ga–N, leading to misaligned nucleation seeds. Other types of N-doping also induced significant deviations, distorting the periodicity of surface ρ distributions, as shown in plan-view maps (Figure 5f–i). In detail, the cross-sectional CDD contour maps (bottom panels of Figure 5e–i) show that the cationic feature on C-on-Al (white dotted lines) and anionic feature on C-on-O (black dotted lines) were partially lost. These deviations near the doped sites disrupt remote epitaxial interactions, leading to the nucle-

ation of epitaxially misaligned adatoms in the early growth stage of anchored remote epitaxy. However, as the growth goes on, the pristine graphene regions, the crystallites encounter regular remote epitaxial interactions, which drive re-alignment. This process explains why anchored remote epitaxy resulted in only small-angle misaligned crystallites. These findings suggest that even minimal atomic doping in single-layer graphene can significantly impact remote epitaxial alignment and compromise the overall homogeneity of the epilayer. Notably, anchored remote epitaxy differs from the quasi-van der Waals epitaxy observed on N-doped graphene. Liu et al. reported that in the GaN/graphene system on an underlying glass substrate, chemical bonding between GaN and graphene establishes a direct epitaxial relationship.^[30] If our experiments followed the quasi-van der Waals epitaxy mechanism, GaN crystallite alignment should have been confined to individual graphene domains. However, the XRD pole figure measurement confirmed that

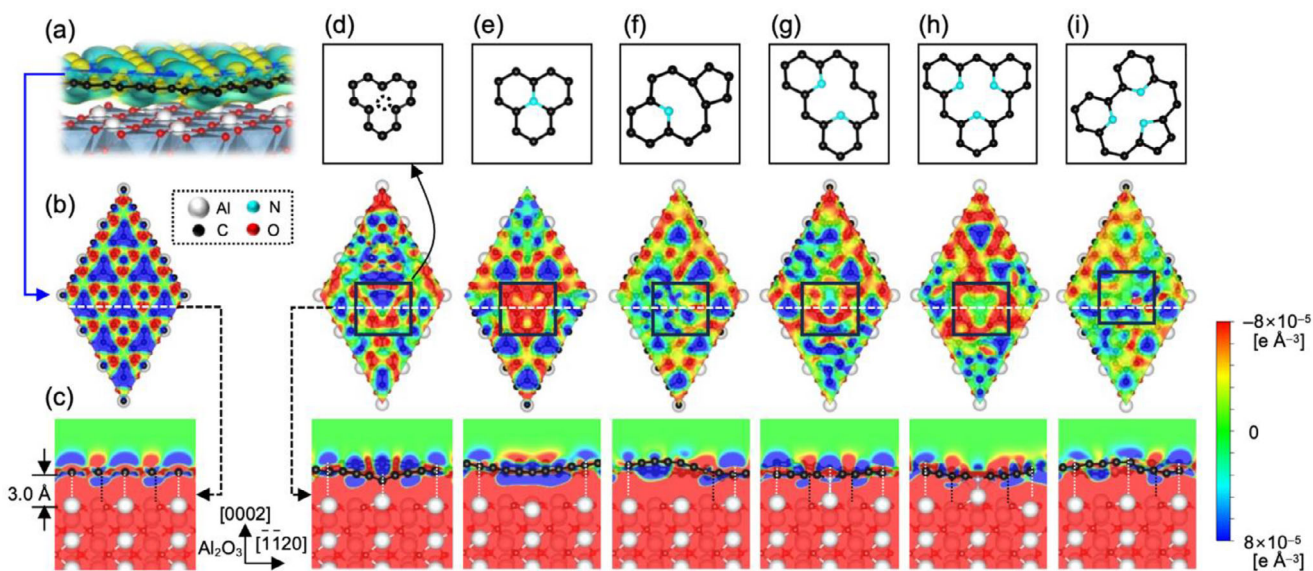


Figure 5. Remote atomic interaction through graphene. DFT-simulated surface charge (ρ) distributions on graphene/Al₂O₃. a–c) Atomic configurations and charge density difference (CDD) isosurface and contour maps: Tilted view of CDD isosurface around pristine graphene (a); Plan-view CDD contour map on the graphene surface (b); Cross-sectional CDD contour map (c), sectioned along the dotted line in (b). d–i) Atomic structures (top), plan-view CDD contour maps (middle), and cross-sectional CDD contour maps (bottom) for graphene with a single carbon vacancy (d), substitutional graphitic nitrogen (e), mono-pyridine (f), dimer-pyridine (g), trimer-pyridine (h), and trimer-pyrrole (i). The white and black dotted lines indicate structural correlation of cationic ρ on C-on-Al (white) and anionic ρ on C-on-O (black). As this correlation was disrupted, the dotted lines were omitted.

alignment was uniform across the entire graphene-coated Al_2O_3 substrate (Figure 3h).

3. Conclusion

This study elucidates how nanoscale defects in graphene determine the epitaxy modes and key characteristics of graphene-assisted GaN epitaxy for the early growth stage. It also contributes to the broader understanding of 2dM-assisted epitaxy and offers practical design principles for optimizing interfacial quality in various remote epitaxy systems. Pristine graphene enables remote epitaxy of well-aligned, strain-relaxed GaN crystallites by mirroring the regular surface charge pattern of the cationic and anionic periodicity of the Al_2O_3 substrate. This mirrored regularity ensures efficient remote epitaxial interaction without chemical bonds, as confirmed by the absence of bonding signatures between GaN and graphene. Conversely, graphene doping hinders the charge transfer fidelity. The doped sites promote high-density chemical anchoring and simultaneously disrupt remote epitaxial interactions. As a result, anchored remote epitaxy yields lots of less aligned epilayer crystallites. However, the absence of direct covalent bonds between GaN and Al_2O_3 still minimizes strain in anchored remote epitaxy. Our results show that remote epitaxial relationships can be maintained even with chemically modified graphene, although chemical anchoring with GaN induces slight epitaxial misalignment. Meanwhile, ELOG achieves good epitaxial alignment via pinhole-mediated covalent bonding but introduces greater in-plane compressive strain due to GaN– Al_2O_3 lattice mismatch. Accordingly, the quality of graphene is critical for nucleation density, crystallographic alignment, strain relaxation, and overall epilayer quality in the graphene-assisted GaN epitaxy.

Beyond the intrinsic requirements, such as preparing a uniform 2dM thickness and selecting suitable substrates, the thermochemical vulnerability of graphene to process-induced damage remains a major challenge for remote epitaxy. Highly reactive and harsh conditions in various epitaxy techniques—such as plasma-assisted molecular beam epitaxy, pulsed laser deposition, and sputtering deposition—are known to introduce defects and damage to 2dMs. Similarly, in oxide remote epitaxy, oxygen exposure during growth can oxidize the 2dM surface, further compromising the fidelity of remote epitaxy. It has been widely believed that achieving successful remote epitaxy merely requires 2dM (or graphene) to be thin and uniform in thickness. However, our study suggests that, in addition to these factors, a chemically undoped, pure 2dM composition is also essential. Therefore, preserving the pristine, intrinsic quality of 2dMs while optimizing epitaxy conditions is critical for achieving successful remote epitaxy. In this regard, our findings highlight the strong correlation between 2dM quality and early-stage epilayer characteristics and provide knowledge into strategies for maintaining the pristine quality of graphene in remote epitaxy. Furthermore, although this study focuses on early-stage epitaxial growth, the insights gained here—particularly regarding strain relaxation and interfacial decoupling—can be extended to growth of freestanding GaN membranes via remote epitaxy. Overall, this work provides meaningful guidance for advancing remote epitaxy by clarifying the role of 2dMs and offering practical strategies for high-quality epilayer membrane fabrication and the related applications.

4. Experimental Section

MOCVD Growth of GaN and Substrate Preparation: GaN crystallites were grown using MOCVD (SYSNEC Co., Marvel 260s). H_2 served as the carrier gas, while trimethylgallium (TMGa) and NH_3 were employed as the precursors of Ga and N, respectively. For all growth processes, a seed layer was initiated at 450 °C and 200 torr for 10 min. Subsequently, GaN crystallites were grown at designated temperatures of 950 or 1050 °C, as outlined in Figure 1a. For process III, hydrogen-ambient thermal pretreatment was performed at 1130 °C prior to initiating seed growth.

Poly-domain graphene (LG Graphene Co., Ltd.), synthesized by CVD on Cu foil, was transferred onto a *c*-plane Al_2O_3 wafer using a wet transfer method. To precisely control graphene defects, we employed α - Al_2O_3 (0001) substrate, which exhibits significantly higher thermal and chemical stability compared to AlN or GaN.^[44,50] This superior stability minimizes graphene degradation associated with substrate decomposition or interfacial reactions during high-temperature growth processes, thereby enabling reproducible defect engineering in graphene layers.^[47,48] Prior to the transfer, the sapphire wafer was annealed in a H_2 atmosphere at 1130 °C for 5 min. For the wet transfer process, poly(methyl methacrylate) (PMMA) was spin-coated onto the graphene on Cu foil at 3000 rpm for 60 s. The Cu foil was subsequently removed by etching in FeCl_3 solution, cleaned with deionized water, and transferred onto the Al_2O_3 wafer. The PMMA/graphene layer was air-dried at room temperature for 24 h and then cleaned in acetone at 80 °C for 40 min to remove PMMA.

Electron Microscopic and Spectroscopic Analyses: The surface morphology of the samples was examined using field-emission scanning electron microscopy (FE-SEM, ThermoFisher Scientific Co., Verios 5 UC) with secondary electron and back-scattered electron imaging modes at an acceleration voltage of 10 kV. Surface coverage and crystallite size distributions were analyzed from the SEM images using ImageJ software.

Aberration-corrected TEM and STEM (ThermoFisher Scientific Co., Spectra Ultra) analyses were performed at an acceleration voltage of 300 kV. Thin cross-sections of specimens were prepared using a focused ion beam (FIB) system (ThermoFisher Scientific Co., Helios 5UX) with a conventional lift-out method. Specimens were extracted using a Ga^+ ion beam at an acceleration voltage of 30 kV for lift-out and sequentially thinned at 16, 5, and 2 kV to minimize damage at the GaN/graphene/ Al_2O_3 interface. STEM-HAADF images were acquired with a convergence angle of 21.5 mrad, a collection angle of 60–220 mrad, and a pixel acquisition time of 3 μs using a resolution of 2K. STEM-EELS measurements were conducted to observe the electronic structure at the epilayer/substrate interface. The energy resolution of EELS, as determined by the full width at half maximum (FWHM) of the zero-loss peak, was 0.8 eV, with an energy dispersion of 90 meV per channel for elemental quantification and fine structure analysis. EELS signals were collected using a direct electron counter (Gatan, K3) with a pixel time of 1 ms. Strain mapping was performed using GPA with commercially available software (HREM Research, GPA). The fundamental principles of GPA applied to atomic-resolution images are described in detail in.^[63] To minimize image distortion and accurately extract both in-plane (ϵ_{xx}) and out-of-plane (ϵ_{yy}) strain components, two HAADF-STEM images were acquired with orthogonal scan directions (90° apart). Prior to strain analysis, a local 2D Wiener filter (HREM Research, Filters Pro) was applied to suppress background noise and enhance lattice contrast. To enable consistent strain comparison across a large area, multiple HAADF-STEM images were seamlessly stitched together. The reference region was defined as the GaN grown on pristine graphene. FFTs were performed using a virtual aperture with a 1 nm^{-1} diameter to isolate the (0001) and (−1−120) diffraction spots, which were then used to calculate the geometric phase corresponding to the respective lattice planes. The aperture size was selected an optimal balance between spatial resolution and signal-to-noise ratio.^[64]

Raman spectroscopic measurements were performed using a 514 nm excitation laser (Renishaw, InVia Raman Microscope). Calibration was conducted with a silicon standard sample prior to measurements. The surface morphology of the graphene/ Al_2O_3 was characterized using AFM in non-contact mode (Park Systems Co., XE-Bio). XRD measurements were

performed through 2θ scans ranging from 20° to 80° with a step width of 0.02° . RSM was carried out around GaN(105) diffraction with a step width of $2\theta/\omega$ and ω at 0.004° . Samples were precisely aligned to the sapphire wafer to minimize geometric errors.

Computational Simulation: The DFT calculations were performed using the Vienna Ab initio Simulation Package (VASP)^[65,66] employing the projector augmented-wave (PAW) method with generalized gradient approximation (GGA) under the Perdew–Burke–Ernzerhof (PBE) framework.^[67,68] Grimme's DFT–D3 method was applied for the van der Waals corrections.^[69] The graphene/c-Al₂O₃ substrate was modeled with $6 \times 6 \times 1$ monolayer graphene and a $3 \times 3 \times 1$ Al₂O₃ (0001) slab of 12 \AA thickness, separated by a vacuum region of 20 \AA . For simplification, the in-plane alignment was set to $[1-100]_{\text{graphene}} \parallel [1-100]_{\text{sapphire}}$. To minimize lattice mismatches, graphene was strained by -1.6% . The plane-wave basis set was expanded to a cutoff energy of 520 eV to minimize Pulay stress during structural optimization. The optimization process was truncated when the Hellmann–Feynman forces were reduced to less than 0.01 eV \AA^{-1} , with electronic energy convergence set to $1 \times 10^{-5} \text{ eV}$. A Γ -centered k-point mesh of $2 \times 2 \times 1$ was employed to set the Brillouin zone. The charge density (ρ) was estimated by calculating $\rho_{\text{graphene/sapphire}} - \rho_{\text{graphene}}$, where $\rho_{\text{graphene/sapphire}}$ and ρ_{graphene} are the charge densities of graphene/Al₂O₃ and graphene, respectively.

Supporting Information

Supporting Information is available from the Wiley Online Library or from the author.

Acknowledgements

This work was supported by the National Research Foundation of Korea (NRF) grant funded by the Korea government (MSIT) (NRF-2022M3D1A2050793 and NRF-2022R1A2C2012462) and Samsung Display Co., Ltd. The work of Y.J.H. was financially supported by the Ministry of Trade, Industry, and Energy (MOTIE) of Korea, supervised by the Korea Institute for Advancement of Technology (KIAT, P0028512 and RS-2024-00418086) and the Korea Planning & Evaluation Institute of Industrial Technology (KEIT, RS-2024-00420767 and RS-2024-00417435). This work of S.H.O. was supported by the Technology Innovation Program (RS-2024-00418991) funded by the MOTIE. The TEM at KENTECH was supported by the Center for Shared Research Facilities.

Conflict of Interest

The authors declare no conflict of interest.

Data Availability Statement

The data that support the findings of this study are available from the corresponding author upon reasonable request.

Keywords

defect, GaN, graphene, MOCVD, remote epitaxy

Received: March 17, 2025

Revised: July 23, 2025

Published online: August 18, 2025

[1] J. E. Ayers, T. Kujofsa, P. Rago, J. E. Raphael, *Heteroepitaxy of Semiconductors: Theory, Growth, and Characterization*, CRC Press, Taylor & Francis Group, Boca Raton, **2017**, 659.

- [2] K. Chung, C.-H. Lee, G.-C. Yi, *Science* **2010**, *330*, 655.
- [3] Y. Kobayashi, K. Kumakura, T. Akasaka, T. Makimoto, *Nature* **2012**, *484*, 223.
- [4] J. Kim, C. Bayram, H. Park, C.-W. Cheng, C. Dimitrakopoulos, J. A. Ott, K. B. Reuter, S. W. Bedell, D. K. Sadana, *Nat. Commun.* **2014**, *5*, 4836.
- [5] Y. Kim, S. S. Cruz, K. Lee, B. O. Alawode, C. Choi, Y. Song, J. M. Johnson, C. Heidelberger, W. Kong, S. Choi, K. Qiao, I. Almansouri, E. A. Fitzgerald, J. Kong, A. M. Kolpak, J. Hwang, J. Kim, *Nature* **2017**, *544*, 340.
- [6] H. Kim, C. S. Chang, S. Lee, J. Jiang, J. Jeong, M. Park, Y. Meng, J. Ji, Y. Kwon, X. Sun, W. Kong, H. S. Kum, S.-H. Bae, K. Lee, Y. J. Hong, J. Shi, J. Kim, *Nat. Rev. Methods Primers* **2022**, *2*, 40.
- [7] H. Kim, Y. Liu, K. Lu, C. S. Chang, D. Sung, M. Akl, K. Qiao, K. S. Kim, B.-I. Park, M. Zhu, J. M. Suh, J. Kim, J. Jeong, Y. Baek, Y. J. Ji, S. Kang, S. Lee, N. M. Han, C. Kim, C. Choi, X. Zhang, H.-K. Choi, Y. Zhang, H. Wang, L. Kong, N. N. Afeefah, M. N. M. Ansari, J. Park, K. Lee, G. Y. Yeom, et al., *Nat. Nanotechnol.* **2023**, *18*, 464.
- [8] M. M. Shulaker, T. F. Wu, M. M. Sabry, H. Wei, H.-S. P Wong, S. Mitra, In *Design, Automation & Test in Europe Conference & Exhibition*, 2015, IEEE Conference Publications, Grenoble, France, **2015**, pp. 1197–1202.
- [9] C.-M. Kang, J.-Y. Lee, D.-J. Kong, J.-P. Shim, S. Kim, S.-H. Mun, S.-Y. Choi, M.-D. Park, J. Kim, D.-S. Lee, *ACS Photonics* **2018**, *5*, 4413.
- [10] S. Mun, C. Kang, J. Min, S. Choi, W. Jeong, G. Kim, J. Lee, K. Kim, H. C. Ko, D. Lee, *Adv. Mater. Interfaces* **2021**, *8*, 2100300.
- [11] J. Shin, H. Kim, S. Sundaram, J. Jeong, B.-I. Park, C. S. Chang, J. Choi, T. Kim, M. Saravanapavanantham, K. Lu, S. Kim, J. M. Suh, K. S. Kim, M.-K. Song, Y. Liu, K. Qiao, J. H. Kim, Y. Kim, J.-H. Kang, J. Kim, D. Lee, J. Lee, J. S. Kim, H. E. Lee, H. Yeon, H. S. Kum, S.-H. Bae, V. Bulovic, K. J. Yu, K. Lee, et al., *Nature* **2023**, *614*, 81.
- [12] D. Holec, Y. Zhang, D. V. S. Rao, M. J. Kappers, C. McAleese, C. J. Humphreys, *J. Appl. Phys.* **2008**, *104*, 123514.
- [13] S.-H. Bae, K. Lu, Y. Han, S. Kim, K. Qiao, C. Choi, Y. Nie, H. Kim, H. S. Kum, P. Chen, W. Kong, B.-S. Kang, C. Kim, J. Lee, Y. Baek, J. Shim, J. Park, M. Joo, D. A. Muller, K. Lee, J. Kim, *Nat. Nanotechnol.* **2020**, *15*, 272.
- [14] B. Liu, Q. Chen, Z. Chen, S. Yang, J. Shan, Z. Liu, Y. Yin, F. Ren, S. Zhang, R. Wang, M. Wu, R. Hou, T. Wei, J. Wang, J. Sun, J. Li, Z. Liu, Z. Liu, P. Gao, *Nano Lett.* **2022**, *22*, 3364.
- [15] B. Shi, Z. Liu, Y. Li, Q. Chen, J. Liu, K. Yang, M. Liang, X. Yi, J. Wang, J. Li, J. Kang, P. Gao, Z. Liu, *Nano Lett.* **2024**, *24*, 7458.
- [16] J. Jiang, X. Sun, X. Chen, B. Wang, Z. Chen, Y. Hu, Y. Guo, L. Zhang, Y. Ma, L. Gao, F. Zheng, L. Jin, M. Chen, Z. Ma, Y. Zhou, N. P. Padture, K. Beach, H. Terrones, Y. Shi, D. Gall, T.-M. Lu, E. Wertz, J. Feng, J. Shi, *Nat. Commun.* **2019**, *10*, 4145.
- [17] T. Journot, H. Okuno, N. Mollard, A. Michon, R. Dagher, P. Gergaud, J. Dijon, A. V. Kolobov, B. Hyot, *Nanotechnology* **2019**, *30*, 505603.
- [18] W. Kong, H. Li, K. Qiao, Y. Kim, K. Lee, Y. Nie, D. Lee, T. Osadchy, R. J. Molnar, D. K. Gaskill, R. L. Myers-Ward, K. M. Daniels, Y. Zhang, S. Sundaram, Y. Yu, S. Bae, S. Rajan, Y. Shao-Horn, K. Cho, A. Ougazzaden, J. C. Grossman, J. Kim, *Nat. Mater.* **2018**, *17*, 999.
- [19] J. Jeong, Q. Wang, J. Cha, D. K. Jin, D. H. Shin, S. Kwon, B. K. Kang, J. H. Jang, W. S. Yang, Y. S. Choi, J. Yoo, J. K. Kim, C.-H. Lee, S. W. Lee, A. Zakhidov, S. Hong, M. J. Kim, Y. J. Hong, *Sci. Adv.* **2020**, *6*, 5180.
- [20] F. Liu, T. Wang, X. Gao, H. Yang, Z. Zhang, Y. Guo, Y. Yuan, Z. Huang, J. Tang, B. Sheng, Z. Chen, K. Liu, B. Shen, X.-Z. Li, H. Peng, X. Wang, *Sci. Adv.* **2023**, *9*, 8484.
- [21] P. Vuong, T. Moudakir, R. Gujrati, A. Srivastava, V. Ottapilakkal, S. Gautier, P. L. Voss, S. Sundaram, J. P. Salvestrini, A. Ougazzaden, *Adv. Mater. Technol.* **2023**, *8*, 2300600.
- [22] J. Jeong, K.-A. Min, B. K. Kang, D. H. Shin, J. Yoo, W. S. Yang, S. W. Lee, S. Hong, Y. J. Hong, *Appl. Phys. Lett.* **2018**, *113*, 233103.

- [23] C. S. Chang, K. S. Kim, B.-I. Park, J. Choi, H. Kim, J. Jeong, M. Barone, N. Parker, S. Lee, X. Zhang, K. Lu, J. M. Suh, J. Kim, D. Lee, N. M. Han, M. Moon, Y. S. Lee, D.-H. Kim, D. G. Schlom, Y. J. Hong, J. Kim, *Sci. Adv.* **2023**, *9*, 5379.
- [24] Y. Wang, Y. Qu, Y. Xu, D. Li, Z. Lu, J. Li, X. Su, G. Wang, L. Shi, X. Zeng, J. Wang, B. Cao, K. Xu, *ACS Nano* **2023**, *17*, 4023.
- [25] X. Wang, J. Choi, J. Yoo, Y. J. Hong, *Nano Converg.* **2023**, *10*, 40.
- [26] J. Jeong, K.-A. Min, D. H. Shin, W. S. Yang, J. Yoo, S. W. Lee, S. Hong, Y. J. Hong, *Nanoscale* **2018**, *10*, 22970.
- [27] J. Jeong, D. K. Jin, J. Cha, B. K. Kang, Q. Wang, J. Choi, S. W. Lee, V. Y. Mikhailovskii, V. Neplokh, N. Amador-Mendez, M. Tchernycheva, W. S. Yang, J. Yoo, M. J. Kim, S. Hong, Y. J. Hong, *ACS Appl. Nano Mater.* **2020**, *3*, 8920.
- [28] H. Kim, K. Lu, Y. Liu, H. S. Kum, K. S. Kim, K. Qiao, S.-H. Bae, S. Lee, Y. J. Ji, K. H. Kim, H. Paik, S. Xie, H. Shin, C. Choi, J. H. Lee, C. Dong, J. A. Robinson, J.-H. Lee, J.-H. Ahn, G. Y. Yeom, D. G. Schlom, J. Kim, *ACS Nano* **2021**, *15*, 10587.
- [29] S. Lee, J. Kim, B.-I. Park, H. I. Kim, C. Lim, E. Lee, J. Y. Yang, J. Choi, Y. J. Hong, C. S. Chang, H. S. Kum, J. Kim, K. Lee, H. Kim, G.-C. Yi, *Appl. Phys. Lett.* **2024**, *125*, 252102.
- [30] F. Liu, Z. Zhang, X. Rong, Y. Yu, T. Wang, B. Sheng, J. Wei, S. Zhou, X. Yang, F. Xu, Z. Qin, Y. Zhang, K. Liu, B. Shen, X. Wang, *Adv. Funct. Mater.* **2020**, *30*, 2001283.
- [31] F. Liu, T. Wang, Z. Zhang, T. Shen, X. Rong, B. Sheng, L. Yang, D. Li, J. Wei, S. Sheng, X. Li, Z. Chen, R. Tao, Y. Yuan, X. Yang, F. Xu, J. Zhang, K. Liu, X. Li, B. Shen, X. Wang, *Adv. Mater.* **2022**, *34*, 2106814.
- [32] S. Strite, M. E. Lin, H. Morkoç, *Thin Solid Films* **1993**, *231*, 197.
- [33] L. Ardaravičius, A. Matulionis, J. Liberis, O. Kiprijanovic, M. Ramonas, L. F. Eastman, J. R. Shealy, A. Vertiatchikh, *Appl. Phys. Lett.* **2003**, *83*, 4038.
- [34] H. Amano, *Jpn. J. Appl. Phys.* **2013**, *52*, 050001.
- [35] A. Hassan, Y. Savaria, M. Sawan, *IEEE Access* **2018**, *6*, 78790.
- [36] S. H. Choi, Y. Kim, I. Jeon, H. Kim, *Adv. Mater.* **2024**, 2411108.
- [37] S. Bao, Y. Wang, K. Lina, L. Zhang, B. Wang, W. A. Sasangka, K. E. K. Lee, S. J. Chua, J. Michel, E. Fitzgerald, C. S. Tan, K. H. Lee, *J. Semicond.* **2021**, *42*, 023106.
- [38] M. H. Doan, S. Kim, J. J. Lee, H. Lim, F. Rotermund, K. Kim, *AIP Adv.* **2012**, *2*, 022122.
- [39] C.-W. Cheng, K.-T. Shiu, N. Li, S.-J. Han, L. Shi, D. K. Sadana, *Nat. Commun.* **2013**, *4*, 1577.
- [40] H. Kum, D. Lee, W. Kong, H. Kim, Y. Park, Y. Kim, Y. Baek, S.-H. Bae, K. Lee, J. Kim, *Nat. Electron.* **2019**, *2*, 439.
- [41] S. Choo, S. Varshney, H. Liu, S. Sharma, R. D. James, B. Jalan, *Sci. Adv.* **2024**, *10*, 8561.
- [42] B.-I. Park, J. Kim, K. Lu, X. Zhang, S. Lee, J. M. Suh, D.-H. Kim, H. Kim, J. Kim, *Nano Lett.* **2024**, *24*, 2939.
- [43] S. Bae, H. Kim, Y. Lee, X. Xu, J.-S. Park, Y. Zheng, J. Balakrishnan, T. Lei, H. Ri Kim, Y. I. Song, Y.-J. Kim, K. S. Kim, B. Özyilmaz, J.-H. Ahn, B. H. Hong, S. Iijima, *Nat. Nanotechnol.* **2010**, *5*, 574.
- [44] J. Park, J. Lee, M. Park, J. Min, J. Lee, X. Yang, S. Kang, S. Kim, W. Jeong, H. Amano, D. Lee, *Adv. Mater. Interfaces* **2019**, *6*, 1900821.
- [45] X. Han, J. Yu, Z. Li, X. Wang, Z. Hao, Y. Luo, C. Sun, Y. Han, B. Xiong, J. Wang, H. Li, Y. Zhang, B. Duan, J. Ning, H. Wu, L. Wang, *ACS Appl. Electron. Mater.* **2022**, *4*, 5326.
- [46] X. Han, J. Yu, P. Yang, B. Liu, X. Wang, Z. Hao, Y. Luo, C. Sun, Y. Han, B. Xiong, J. Wang, H. Li, L. Wang, *ACS Appl. Nano Mater.* **2023**, *6*, 15159.
- [47] H.-M. Kwak, J.-S. Lee, B.-I. Park, J. Baik, J. Kim, W.-L. Jeong, K.-P. Kim, S.-H. Mun, H. Kim, J. Kim, D.-S. Lee, *ACS Nano* **2023**, *17*, 11739.
- [48] J. Choi, J. Jeong, X. Zhu, J. Kim, B. K. Kang, Q. Wang, B.-I. Park, S. Lee, J. Kim, H. Kim, J. Yoo, G.-C. Yi, D.-S. Lee, J. Kim, S. Hong, M. J. Kim, Y. J. Hong, *ACS Nano* **2023**, *17*, 21678.
- [49] H.-M. Kwak, J. Kim, J.-S. Lee, J. Kim, J. Baik, S.-Y. Choi, S. Shin, J.-S. Kim, S.-H. Mun, K.-P. Kim, S. H. Oh, D.-S. Lee, *ACS Appl. Mater. Interfaces* **2023**, *15*, 59025.
- [50] J.-H. Park, X. Yang, J.-Y. Lee, M.-D. Park, S.-Y. Bae, M. Pristovsek, H. Amano, D.-S. Lee, *Chem. Sci.* **2021**, *12*, 7713.
- [51] X. Li, Y. Zhu, W. Cai, M. Borysiak, B. Han, D. Chen, R. D. Piner, L. Colombo, R. S. Ruoff, *Nano Lett.* **2009**, *9*, 4359.
- [52] G. Sarau, M. Heilmann, M. Bashouti, M. Latzel, C. Tessarek, S. Christiansen, *ACS Appl. Mater. Interfaces* **2017**, *9*, 10003.
- [53] H. Schulz, K. H. Thiemann, *Solid State Commun.* **1977**, *23*, 815.
- [54] T. Detchprohm, K. Hiramatsu, K. I. Kenji Itoh, I. A. Isamu Akasaki, *Jpn. J. Appl. Phys.* **1992**, *31*, 1454.
- [55] V. S. Harutyunyan, A. P. Aivazyan, E. R. Weber, Y. Kim, Y. Park, S. G. Subramanya, *J. Phys. D: Appl. Phys.* **2001**, *34*, 35.
- [56] S. Tomiya, K. Funato, T. Asatsuma, T. Hino, S. Kijima, T. Asano, M. Ikeda, *Appl. Phys. Lett.* **2000**, *77*, 636.
- [57] G. Feng, X. H. Zheng, Y. Fu, J. J. Zhu, X. M. Shen, B. S. Zhang, D. G. Zhao, Y. T. Wang, H. Yang, J. W. Liang, *J. Cryst. Growth* **2002**, *240*, 368.
- [58] H. Kim, S. Lee, J. Shin, M. Zhu, M. Akl, K. Lu, N. M. Han, Y. Baek, C. S. Chang, J. M. Suh, K. S. Kim, B.-I. Park, Y. Zhang, C. Choi, H. Shin, H. Yu, Y. Meng, S.-I. Kim, S. Seo, K. Lee, H. S. Kum, J.-H. Lee, J.-H. Ahn, S.-H. Bae, J. Hwang, Y. Shi, J. Kim, *Nat. Nanotechnol.* **2022**, *17*, 1054.
- [59] J. H. Warner, Y.-C. Lin, K. He, M. Koshino, K. Suenaga, *ACS Nano* **2014**, *8*, 11806.
- [60] Y.-C. Lin, P.-Y. Teng, C.-H. Yeh, M. Koshino, P.-W. Chiu, K. Suenaga, *Nano Lett.* **2015**, *15*, 7408.
- [61] H. Tan, J. Verbeeck, A. Abakumov, G. Van Tendeloo, *Ultramicroscopy* **2012**, *116*, 24.
- [62] S. Lazar, G. A. Botton, M.-Y. Wu, F. D. Tichelaar, H. W. Zandbergen, *Ultramicroscopy* **2003**, *96*, 535.
- [63] M. J. Hytch, E. Snoeck, R. Kilaas, *Ultramicroscopy* **1998**, *74*, 131.
- [64] Y. Zhu, C. Ophus, J. Ciston, H. Wang, *Acta Mater.* **2013**, *61*, 5646.
- [65] G. Kresse, J. Furthmüller, *Phys. Rev. B* **1996**, *54*, 11169.
- [66] G. Kresse, J. Furthmüller, *Comput. Mater. Sci.* **1996**, *6*, 15.
- [67] J. P. Perdew, K. Burke, M. Ernzerhof, *Phys. Rev. Lett.* **1996**, *77*, 3865.
- [68] P. E. Blöchl, *Phys. Rev. B* **1994**, *50*, 17953.
- [69] S. Grimme, J. Antony, S. Ehrlich, H. Krieg, *J. Chem. Phys.* **2010**, *132*, 154104.